Article

Trapping of Rayleigh Spheroidal Particles Using Tightly Focused Higher-Order Vector Vortex Beams

Dong Li *[ID], Hongxu Zhang, Chengquan Wei, Yundi Zhang, Xize Gao, Dandan Wen, Peng Li [ID] and Jianlin Zhao [ID]

MOE Key Laboratory of Material Physics and Chemistry under Extraordinary Conditions,
Shaanxi Key Laboratory of Optical Information Technology, School of Physical Science and Technology,
Northwestern Polytechnical University, Xi'an 710129, China
* Correspondence: dongli@nwpu.edu.cn

Abstract: Considering the advantages of higher-order vector vortex beams (HOVVBs) with their diverse intensity distribution of the focal field and adjustable longitudinal field component, we investigated the optical forces and torques on Rayleigh spheroidal particles induced by tightly focused HOVVBs based on the Rayleigh scattering model and dipole approximation. It was found that the maximal optical forces were obtained when the major axis of the Rayleigh spheroidal particles was parallel to the x–y plane. We achieved the three-dimensional stable trapping of Rayleigh spheroidal particles at the focus by using an HOVVB. Further analysis showed that the optical torque caused the major axis of the spheroidal particle to rotate towards the x–y plane, which is conducive to the large-scale stable trapping of Rayleigh spheroidal particles in the two-dimensional plane. Moreover, the optical torque Γ_x could achieve a maximum of 0.869 pN·nm at $\varphi_0 = 90°$ and 270°, while Γ_y could achieve a maximum of 0.869 pN·nm at $\varphi_0 = 0°$ and 180° for the case of $\theta_0 = 30°$. Our findings provide a clear strategy for extending the degrees of freedom in the control of the beam. We envision a significant role for these results in optical micro-manipulation.

Keywords: higher-order vector vortex beams; Rayleigh spheroidal particles; optical torque

1. Introduction

Due to their unique polarization distribution and novel properties after being tightly focused [1], vector beams have shown huge application potential in the fields of optical computation, information encryption, quantum optical communication, and optical micromanipulation, among others [2–5]. Additionally, the generation of vector beams has also received increasing attention. E. Hasman et al. experimentally obtained a third-order vector light field with a grating structure of triple rotation symmetry [6]. Kang et al.'s study aimed to investigate a radially polarized light field that was generated by etching circular rectangular cracks on gold film [7]. At the same time, optical tweezers [8–11] have attracted great attention in the field of micro-particle manipulation as they offer contact-free manipulation and high accuracy. In the past few decades, several pioneers have analyzed the optical trapping of particles by using various beams. Ashkin et al. demonstrated the optical trapping of dielectric particles by using a single focused laser beam [12]. Zhan et al. used radial polarization vector beams to stably trap metallic particles [13]. Jiang et al. investigated the trapping stability of a dielectric spherical particle using a Lorentz–Gauss beam [14]. With the development of optical micro-manipulation technology, higher requirements have been put forward in the research of beam and particle characteristics. Bi et al. examined the applicability of the ellipsoid model to analyze the scattering properties of realistic aerosol particles by analyzing the feldspar aerosols through theoretical and experimental means. It was found that the triaxial ellipsoidal particle model was better than the commonly used spheroid model for simulating dust particle optical properties, particularly with respect to their realistic polarization characteristics [15]. Many biological particles are non-spherical,

such as red blood cells, chloroplasts, and phospholipid vesicles [16–19]. Elliptical Rayleigh particles have attracted the attention of researchers because they can be used to model several irregular particles, especially cylindrical or disc-shaped particles. Hinojosa et al. analyzed the optical forces and torques from a ringed beam on a prolate spheroid [20]. Cao et al. dynamically simulated the equilibrium orientations of oblate spheroidal particles by using the hybrid discrete-dipole approximation and T-matrix methods [21]. Xu et al. presented theoretical solutions of the radiation force and torque exerted on a spheroid by arbitrarily shaped beams [22]. Rui et al. studied the optical trapping of Rayleigh ellipsoid particles by using a diffraction-limited focusing beam with arbitrary photon spin [23,24]. However, several studies have mainly analyzed the trapping of large-sized spheroidal particles. In particular, the influence of the polarization and phase of the light field on the optical force of Rayleigh spheroidal particles needs to be further analyzed. In this study, we considered higher-order vector vortex beams (HOVVBs), which have diverse intensity distributions in the focused field and adjustable longitudinal components for optical trapping [25–27].

In past decades, the technology of optical tweezers has made significant contributions to various scientific areas, including optics, photonics, and nanosciences. Zou et al. found that optical tweezers could be used to generate a dynamic scanning optical trap along a given circular trajectory, which can trap and drive a microparticle or single cell to move along the trajectory, thus generating a microvortex [28]. Based on the optical force, confocal fluorescence microscopy and microfluidics, one can isolate single macrophages and follow their immediate responses to a biochemical stimulus in real-time. This strategy allows for live-cell imaging at a high spatiotemporal resolution and omits surface adhesion and cell–cell contact as biophysical stimuli [29]. Secondly, optical tweezers also generate a variety of fascinating beam patterns, allowing biologists to uncover the natural secrets of human life at the single-cell level. Due to its gentle treatment and high resolution, this technology opens up a new chapter for cytology studies, ranging from studies investigating cells infected with pathogenic bacteria to those stimulating cell mechanotransduction. Optical tweezers play an irreplaceable role in the field of cytology, including in chromatin analysis, blood diagnosis, cytoskeletal adjustment, intercellular adhesion, single-molecule assessment, and in vitro reconstruction processes [30].

Optical tweezers have shown rapid progress in manipulating particles in recent years. Breakthroughs include manipulating particles in both static and dynamic ways, conducting particle sorting, and constructing controllable micromachines. Advances in shaping and controlling the laser beam profile allows for control over the position and location of the trap, which has many potential applications. A linear optical tweezer can be created by rapidly moving a spot optical tweezer using a tool such as a galvanometer mirror or an acousto-optic modulator. By manipulating the intensity profile along the beam line to be asymmetric or non-uniform, the technique can be applied to various specific fields [31]. Chen et al. researched the optical trapping of polystyrene microspheres. The transverse capture gradient forces of polystyrene microspheres with different numerical apertures were theoretically and experimentally analyzed using the power spectral density roll-off method. It was found that the trapping force of the experimental measurement was much stronger than that of the theoretical results [32]. Shao et al. use infrared optical tweezers to dynamically control the microvascular reperfusion within subdermal capillaries in the pinna of mice [33]. In 2023, Hwang et al. performed much in a study aimed at achieving optical tweezers to throw and capture single atoms [34]; the authors experimentally demonstrated that free-flying atoms are not guided, but rather ejected and trapped by optical tweezers; the authors provided a set of proof-of-principle demonstrations of flying atoms, including atom transport through optical tweezers, atom arrangement through flying atoms, and atom scattering over optical tweezers. These developments makes it possible for individual atoms to move from one place to another, helping to make flying quantum memory possible. In 2023, Ho Quang Quy et al. investigated enhancing optical trapping efficiency by using nonlinear optical tweezers [35]. Remarkably, the optical trapping ef-

ficiency of nonlinear optical tweezers can be enhanced by using an average laser power, and the efficiency can be several times higher than that of the linear optical ones under the same configuration. Wei et al. designed novel cycloid-structured optical tweezers based on modified cycloid and holographic shaping techniques. These optical tweezers realize all of the dynamic characteristics of the trapped particles, including the start, stop, and variable-velocity motions along versatile trajectories [36]. Therefore, our study analyzed the trapping properties of Rayleigh spheroidal particles induced by tightly focused HOVVBs with polarization and phase topological charges $|n| = |m|$ based on the Richards–Wolf vector scattering theory and dipole approximation. The optical force and torque generated by a tightly focused HOVVB on Rayleigh spheroidal particles with different spatial orientations were studied, and the multidimensional optical trapping and manipulation of Rayleigh spheroidal particles were also demonstrated. It was found that unlike linearly polarized and radial vector beams, which can stably trap Rayleigh spheroidal particles in only a certain direction, the HOVVBs can trap the Rayleigh spheroidal particle stably in the entire two-dimensional plane. This discovery can greatly expand the scale of stable trapping for optical tweezers and achieve the three-dimensional stable trapping of Rayleigh spheroidal particles at the focus. Our results would be useful for extending the degrees of freedom of control and the application range of HOVVBs in optical micro-manipulation.

2. Properties of Tightly Focused HOVVBs

According to the Richards–Wolf vectorial diffraction [37,38], the electric field vector of the beam after focusing with a high numerical aperture (NA) lens can be expressed as

$$\mathbf{E}(\mathbf{r}) = \frac{-\mathrm{i}kf}{2\pi} \int_0^{\theta_{\max}} \int_0^{2\pi} \mathbf{A}(\theta, \phi) \exp(\mathrm{i}\mathbf{k} \cdot \mathbf{r}) \sin\theta \, \mathrm{d}\phi \, \mathrm{d}\theta \tag{1}$$

where $k = 2\pi n_1/\lambda_0$ is the wave number in the image space, n_1 and λ_0 are the refractive index and free space wavelength, respectively, f is the focal length, $\theta_{\max}$ is the acceptance angle given by the NA of the objective lens, $\mathbf{k}$ is the wave vector, and $\mathbf{r}$ designates the position vector from the focus to the observation point in the image space. The integral kernel $\mathbf{A}(\theta, \phi)$ is the apodization field [39], which is related to the input field $\mathbf{A_0}(\theta, \phi)$ at the entrance pupil and is expressed as

$$\mathbf{A}(\theta, \phi) = T(\theta) \begin{pmatrix} \mathbf{e}_\theta & 0 \\ 0 & \mathbf{e}_\phi \end{pmatrix} \begin{pmatrix} A_{0r} \\ A_{0\phi} \end{pmatrix} \tag{2}$$

where $T(\theta)$ is the apodization function for an aplanatic lens, $T(\theta) = \cos^{1/2}\theta$, $(\mathbf{e}_\theta, \mathbf{e}_\phi)$ are the unit vectors in the θ and ϕ directions, and $(A_{0\theta}, A_{0\phi})$ are the radial and azimuthal components of the input field $A_0(\theta, \phi)$. The input field of the vector vortex beams [40] can be written as

$$\mathbf{A}_0(\theta, \phi) = l_0 \exp(\mathrm{i}m\phi)\{\cos[(n-1)\phi]\mathbf{e}_r + \sin[(n-1)\phi]\mathbf{e}_\phi\} \tag{3}$$

where n is the polarization topological charge, which means that the polarization direction rotates $2\pi n$ counterclockwise around the beam axis; m is the phase topological charge. $l_0(\theta)$ is the amplitude function [41] and can be assumed to have the form

$$l_0 = \left(\frac{\sqrt{2}\beta_0 \sin\theta}{\sin\theta_{\max}}\right)^m \exp\left[-\left(\frac{\beta_0 \sin\theta}{\sin\theta_{\max}}\right)^2\right] \tag{4}$$

where β_0 is the ratio of the pupil radius to the beam waist.

The components (E_x, E_y, E_z) in cylindrical coordinates (r_s, ϕ_s, z_s) have the following forms [42]:

$$
\begin{aligned}
E_x &= -i^{m+1}e^{im\phi_s}kf\int_0^{\theta_{\max}}\int_0^{2\pi}\sin\theta\cos^{2/3}\theta l_0(\theta)e^{ikz_s\cos\theta}J_m(\beta) \\
&\quad [\cos\phi\cos(\phi-n\phi)+\sin\phi\sin(\phi-n\phi)]\mathrm{d}\phi\mathrm{d}\theta \\
E_y &= -i^{m+1}e^{im\phi_s}kf\int_0^{\theta_{\max}}\int_0^{2\pi}\sin\theta\cos^{2/3}\theta l_0(\theta)e^{ikz_s\cos\theta}J_m(\beta) \\
&\quad [\sin\phi\cos(\phi-n\phi)+\cos\phi\sin(\phi-n\phi)]\mathrm{d}\phi\mathrm{d}\theta \\
E_z &= -i^{m+1}e^{im\phi_s}kf\int_0^{\theta_{\max}}\int_0^{2\pi}\sin^2\theta\cos^{2/3}\theta l_0(\theta)e^{ikz_s\cos\theta}J_m(\beta) \\
&\quad [\cos(\phi-n\phi)]\mathrm{d}\phi\mathrm{d}\theta
\end{aligned}
\tag{5}
$$

From Equation (5), the focusing characteristics of HOVVBs can be obtained. Figure 1 shows the polarization distributions of the HOVVBs with polarization and phase topological charges of $n = m = \pm 3$ and $n = m = \pm 4$ after a lens (NA = 1.26) was placed in water ($n_1 = 1.33$). Here, we assumed that the wavelength and power of the incident beam were $\lambda_0 = 1.053$ μm and $P = 100$ mW, respectively. It can be seen that polarization of the tightly focused HOVVBs is related to the values of n and m. Figure 2 shows the variation in the maximum intensity at the focus with the polarization and phase topological charges ($n = |m| > 1$) for different wavelengths. It can be seen that the intensity maximum of all wavelengths at the focus decreases with the increase in polarization and phase topological charges, and the intensity maximum at the focus also declines with the increase in wavelength for a certain polarization and phase topological charge. Furthermore, it was also found that the intensity maximum at the focus was not affected by the sign of polarization and phase topological charge. Based on this observation, we analyzed the optical forces and torques of tightly focused HOVVBs with $|n| = |m|$ on Rayleigh spheroidal particles.
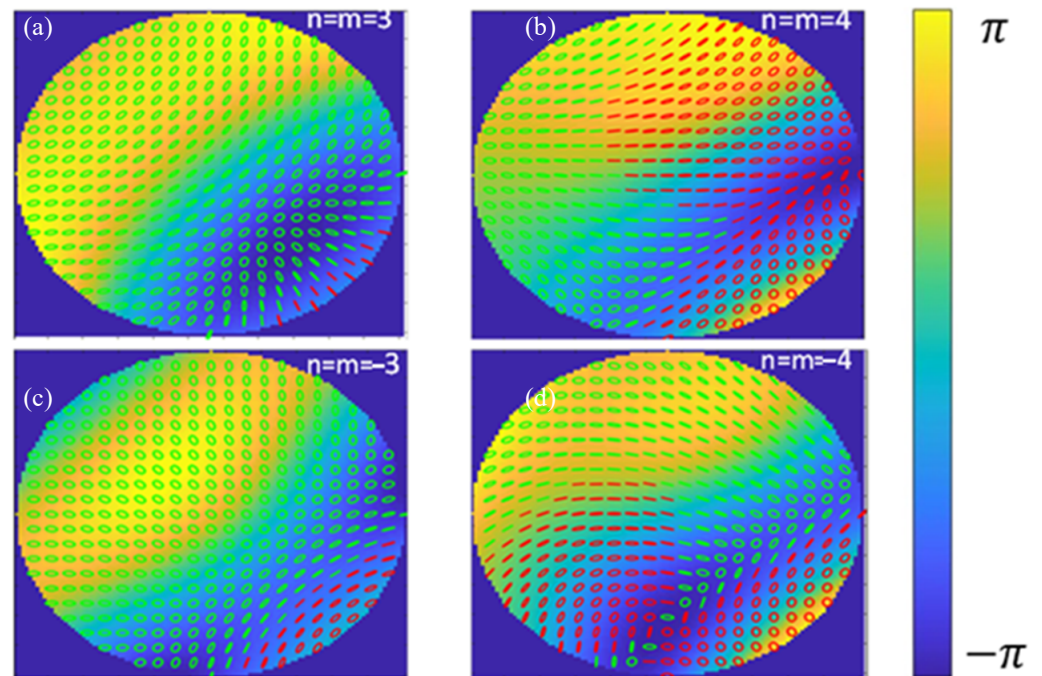
Figure 1. The polarization of tightly focused HOVVBs for different phase topological charges (red circle is the LH polarization, while green circle is the RH polarization). (**a**) $n = m = 3$; (**b**) $n = m = 4$; (**c**) $n = m = -3$; (**d**) $n = m = -4$.
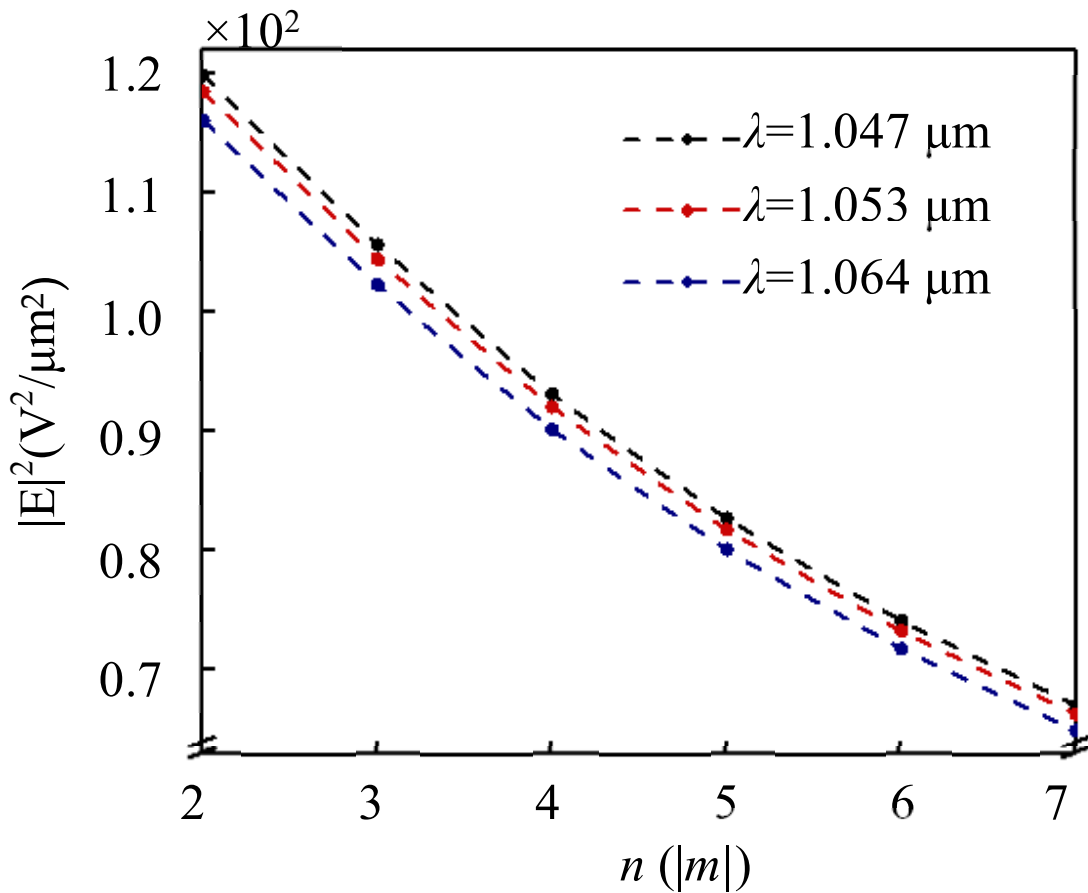
Figure 2. The variation in the maximum intensity at the focus with the polarization and phase topological charges ($n = m > 0$) for different wavelengths.

3. Optical Force and Torque of HOVVBs on Rayleigh Spheroidal Particles

The interaction between the particle and the beam is analyzed by using three physical models according to the general particle size, such as the geometric optics model [43], Rayleigh scattering model, and electromagnetic scattering model [44]. Here, we adopted the Rayleigh scattering model because the size of the Rayleigh spheroidal particle r is far less than wavelength ($r < 0.05\lambda$) in this study. We chose ε_1 and ε_2 ($\varepsilon_1 = \varepsilon_0 n_1^2$, $\varepsilon_2 = \varepsilon_0 n_2^2$) as the dielectric constants of the surroundings around the focused beam and Rayleigh spheroidal particle, respectively. We assumed that the Rayleigh spheroidal particle is much smaller than the wavelength of the incident beam and can be considered as an electric dipole. Considering that the particle is located in the tightly focused beam propagating along the z-axis, a local coordinate system (ξ, η, ζ) with the major and minor axes a and b of the spheroid was established, as shown in Figure 3, to describe the position of the Rayleigh spheroidal particle. ζ is along the major axis a, and θ_0 and φ_0 are the polar and azimuthal angles of the major axis, respectively. The electric dipole moment $\mathbf{p} = \alpha\mathbf{E}$ [45] with the polarizability α [46,47] of a spheroidal particle can be expressed as

$$\left(\alpha_{\delta\gamma}\right) = \begin{pmatrix} \alpha_\xi & 0 & 0 \\ 0 & \alpha_\eta & 0 \\ 0 & 0 & \alpha_\zeta \end{pmatrix}. \tag{6}$$

with

$$\alpha_v = \frac{\alpha_{0v}}{1 - \mathrm{i}2/3k^3\alpha_{0v}}, \tag{7}$$

where $v = \xi, \eta, \zeta$, and α_{0v} is the electrostatic polarizability tensor.
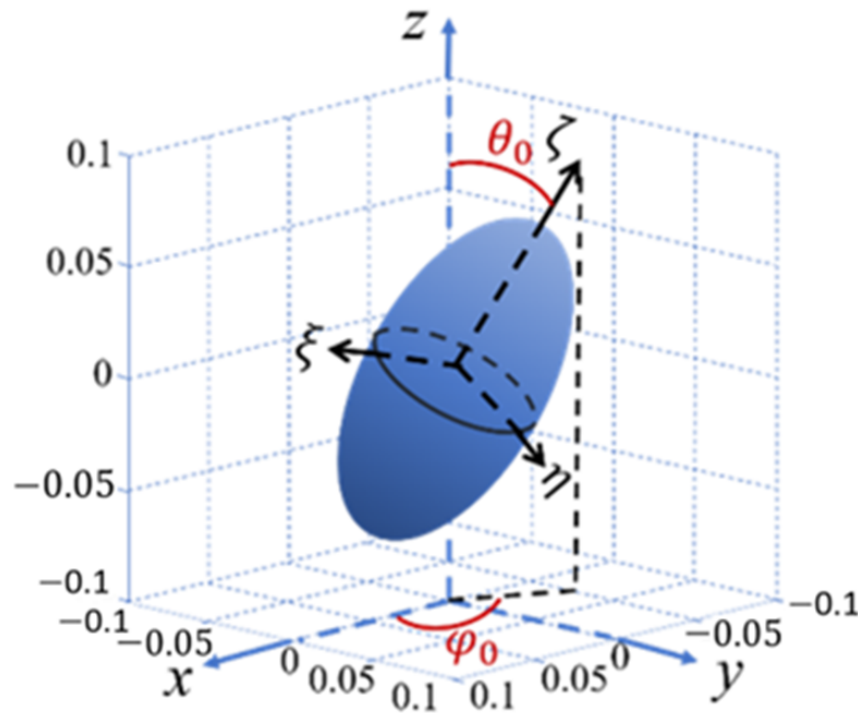
Figure 3. The local coordinate system (ξ, η, ζ) and the spatial orientation of the Rayleigh spheroidal particle.

The susceptibility tensor of the Rayleigh spheroidal particle is affected by its orientation as $(\alpha_{ij}) = (R_{i\delta})(\alpha_{\delta\gamma})(R_{\gamma j})^{-1}$, and the rotation matrix [20,48] R_{ij} can be expressed as

$$R(\theta_0, \varphi_0) = \begin{pmatrix} \cos\varphi_0\cos\theta_0 & -\sin\varphi_0 & \cos\varphi_0\sin\theta_0 \\ \sin\varphi_0\cos\theta_0 & \cos\varphi_0 & \sin\varphi_0\sin\theta_0 \\ -\sin\theta_0 & 0 & \cos\theta_0 \end{pmatrix}. \tag{8}$$

The time-averaged optical force and torque [47,49,50] on the particle is affected by the transfer of the linear and angular momentums from the beam to the particle, which can be expressed as

$$\langle F_i \rangle = \frac{1}{2}\mathrm{Re}\left[p_j \partial_i (E_j)^* \right], \tag{9}$$

$$\langle \mathbf{\Gamma} \rangle = \frac{1}{2}\mathrm{Re}\left[\mathbf{p} \times \left(\alpha_0^{-1} \cdot \mathbf{p} \right)^* \right], \tag{10}$$

where i and j denote the Cartesian components (x, y, z) and * denotes the complex conjugate.

Based on the above analysis, the optical force on the Rayleigh spheroidal particle by using tightly focused HOVVBs were first analyzed for the case where the major axis of the particle is along the z-axis ($\theta_0 = \varphi_0 = 0°$). The refractive index of the Rayleigh spheroidal particle was $n_2 = 1.6$, and the major and minor semi-axes were $a = 50$ nm and $b = 25$ nm, respectively. Figure 4(a1–a3,b1–b3) presents the transverse forces F_x and F_y and the longitudinal force F_z on the Rayleigh spheroidal particles, which is applied by the tightly focused HOVVBs with $n = m = 3$, 4 and $n = m = -3$, -4. It can be seen that the values (instead of the sign) of the polarization and phase topological charges of the HOVVBs have a significant effect on the maxima of the optical forces $F_{x,max}$, $F_{y,max}$, and $F_{z,max}$ on the Rayleigh spheroidal particle. As $|n|$ and $|m|$ increases, $F_{x,max}$, $F_{y,max}$, and $F_{z,max}$ decline. The values of the optical forces on both sides of the focus are the same, and all directions point to the focus, which means that the Rayleigh spheroidal particle can be stably trapped at the focus in three dimensions. Compared with the radial polarization vector vortex beams, which provide stable trapping only in the transverse direction, the

HOVVBs with $|n| = |m|$ can also produce optical forces along the longitudinal direction with the same order of magnitude. Therefore, the stable three-dimensional trapping of Rayleigh spheroidal particles in both the transverse and longitudinal directions can be achieved by using HOVVBs. This discovery will increase the trapping freedom of optical tweezers, which is beneficial for expanding the application scope in the field of optical micro-manipulation.
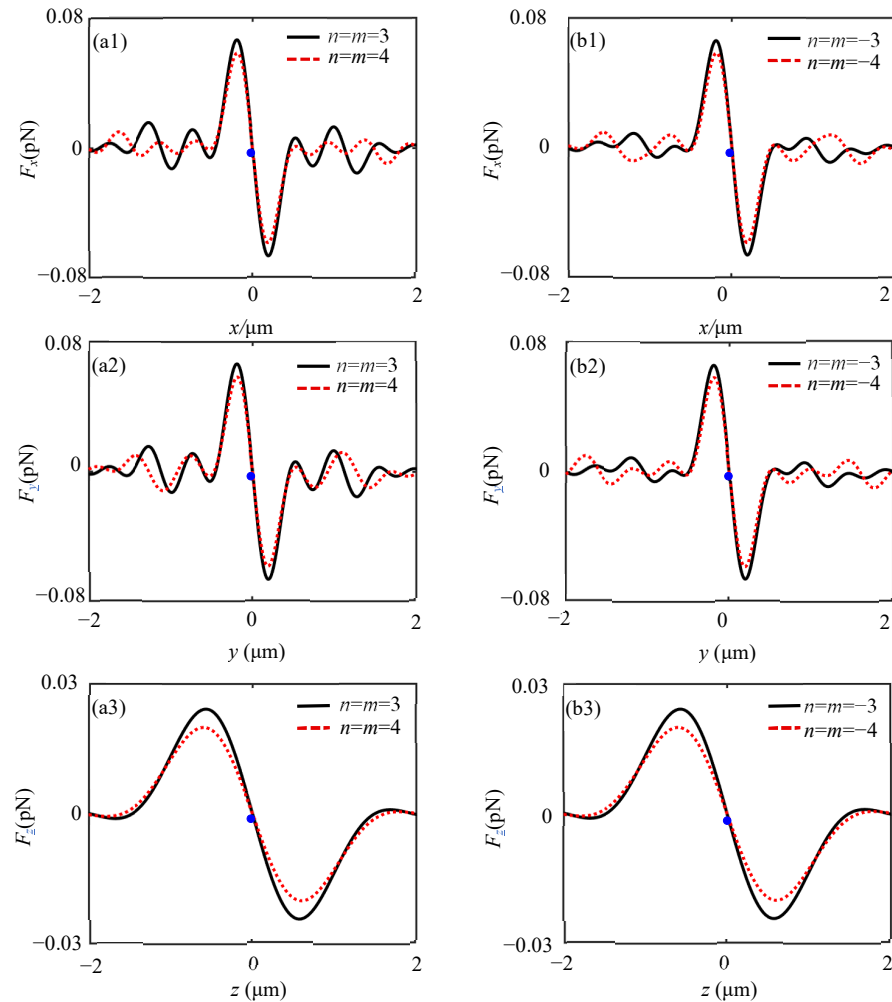
Figure 4. Optical force of HOVVBs on the Rayleigh spheroidal particle (**a1**–**a3**) $n = m = 3$, 4; (**b1**–**b3**) $n = m = -3, -4$. The equilibrium position of the Rayleigh spheroidal particle is indicated by blue dots.

Subsequently, the influence of the polar angle ($0° < \theta_0 < 180°$) and azimuthal angle ($0° < \varphi_0 < 360°$) of Rayleigh spheroidal particles on the maximum value of the optical forces $F_{x,max}$, $F_{y,max}$, and $F_{z,max}$ were also analyzed. Figure 5 shows the evolution of $F_{x,max}$, $F_{y,max}$, and $F_{z,max}$ with the polar and azimuthal angles, and all of the parameters used in the following analysis are the same as those adopted above unless otherwise mentioned. The properties of the optical forces [24] can be described as $G_i \propto \text{Re}[E_x(\sin \theta_0)^2(\cos \varphi_0)^2 \partial_i E_x{}^* + E_y(\sin \theta_0)^2 (\sin \varphi_0)^2 \partial_i E_y{}^* + E_z(\cos \theta_0)^2 \partial_i E_z{}^*]$. It can be seen that $F_{x,max}$, $F_{y,max}$, and $F_{z,max}$ initially increased with the polar angle θ_0 in the range from $0°$ to $90°$ and then declined with the polar angle θ_0 in the range from $90°$ to $180°$ for a certain azimuthal angle φ_0. In other words, the evolution of $F_{x,max}$, $F_{y,max}$, and $F_{z,max}$ was approximately symmetrical with the polar angles $\theta_0 = 90°$ for a certain φ_0. This is because the electric field component E_z at the focus disappears, and $F_{x,max}$, $F_{y,max}$, and $F_{z,max}$ are proportional to $(\sin \theta_0)^2$. Therefore, the maximum values can be obtained at $\theta_0 = 90°$. For certain polar angles θ_0, $F_{x,max}$, and

$F_{y,max}$ show a periodic evolution close to $(\cos \varphi_0)^2$ and $(\sin \varphi_0)^2$, while $F_{z,max}$ is not affected by the azimuthal angles φ_0. Furthermore, $F_{x,max}$, $F_{y,max}$, and $F_{z,max}$ are also not affected by the signs of the polarization and phase topological charges of HOVVBs. Therefore, the stable trapping of Rayleigh spheroidal particles can be achieved for the tightly focused HOVVBs as long as the major axis of the Rayleigh spheroidal particle is parallel to the x–y plane ($\theta_0 = 90°$). Unlike linearly polarized and radial vector beams, which can stably trap Rayleigh spheroidal particles in only a certain direction, HOVVBs can stably trap the Rayleigh spheroidal particle in the entire two-dimensional plane; this discovery can greatly expand the scale of stable trapping for optical tweezers.
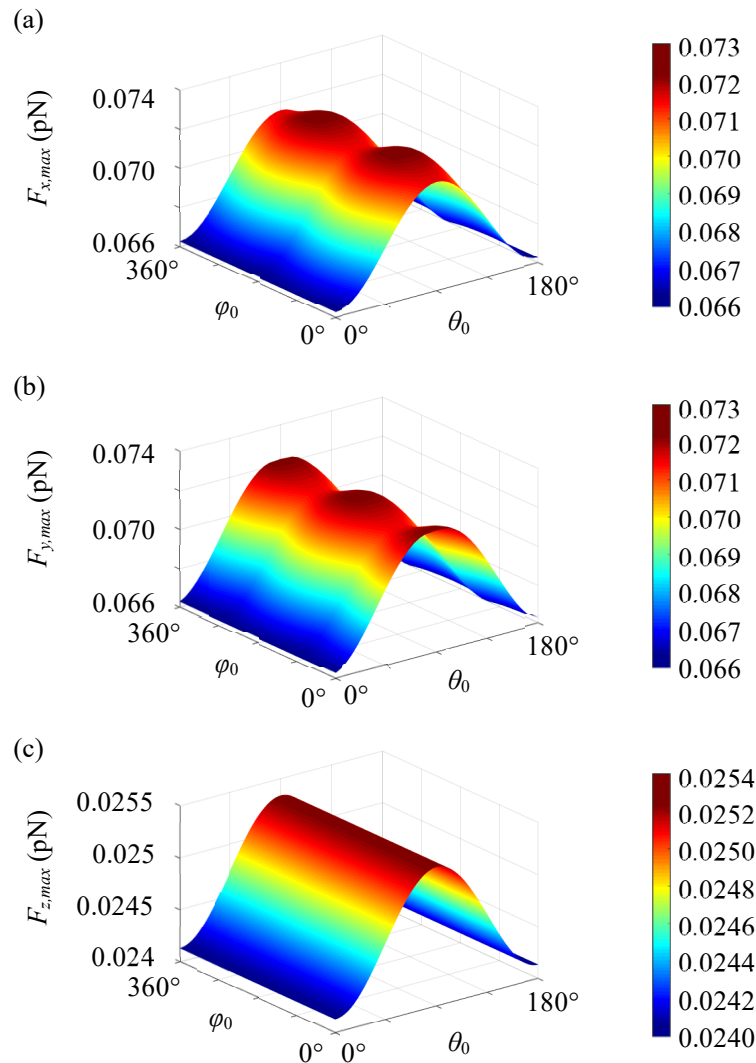

Figure 5. Variation in the maximum value of the optical force (**a**) $F_{x,max}$, (**b**) $F_{y,max,}$, and (**c**) $F_{z,max}$ exerted on Rayleigh spheroidal particle by tightly focused HOVVBs ($n = m = 3$) using the polar and azimuthal angles.

The optical forces on a Rayleigh spheroidal particle will not only move the particle horizontally, but also produce optical torques to promote particle rotation. Therefore, we also analyzed the optical torque properties of Rayleigh spheroidal particles that were induced by the tightly focused HOVVBs. Because of the transverse electric field components $E_x = E_y$ at the focus, the optical torque component Γ_z on the Rayleigh spheroidal particle disappears, while the optical torque exists in the x–y plane for various spatial orientations (θ_0, φ_0) of the Rayleigh spheroidal particle. Figure 6a presents the evolution of the optical torques Γ_x and Γ_y along the x and y axes with φ_0 for the case of $\theta_0 = 30°$. It can be seen

that Γ_x can achieve a maximum of 0.869 pN·nm at $\varphi_0 = 90°$ and $270°$, while Γ_y can achieve a maximum of 0.869 pN·nm at $\varphi_0 = 0°$ and $180°$. Thus, the value of the total transverse optical torque $\Gamma_t = (\Gamma_x{}^2 + \Gamma_y{}^2)^{1/2}$ is a constant. Figure 6b shows the evolution of Γ_x and Γ_y with θ_0 for the case of $\varphi_0 = 30°$. It can be seen that both Γ_x and Γ_y can achieve the maxima at $\theta_0 = 45°$ and $135°$ (the maxima of Γ_x and Γ_y are 0.502 pN·nm and 0.869 pN·nm), and the evolution of Γ_x and Γ_y are dependent on $-\sin(2\theta_0)$ and $\sin(2\theta_0)$, respectively. We define the orientation angle Φ to represent the angle between the torque and the x-axis. The azimuthal angle φ_0 is the included angle between the projection of the axis ζ in the x–y plane and the x-axis. Then, the relation $\tan\Phi = \tan(\varphi_0 + \pi/2)$ can be established, which means that the optical torque is orthogonal to the projection of axis ζ in the x–y plane. In summary, the directions of the optical torques Γ_x and Γ_y are dependent on φ_0, and their evolution is approximately proportional to the sine function of θ_0 for a certain φ_0. Similarly, the evolution of the optical torques Γ_x and Γ_y with θ_0 and φ_0 is not dependent on the signs of polarization and phase topological charges. Therefore, the stable trapping of Rayleigh spheroidal particles can be achieved when the axis ζ is parallel to the x–y plane.
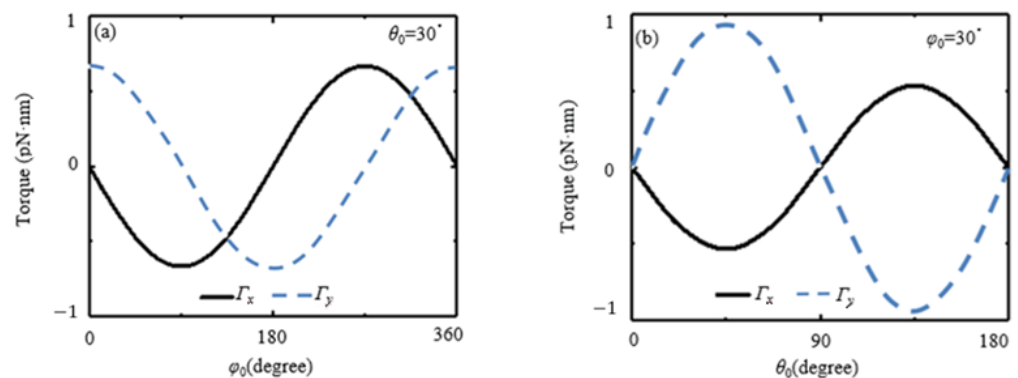

Figure 6. The variation in the torques Γ_x and Γ_y on the Rayleigh spheroidal particle at the focus using the polar and azimuthal angles. (**a**) The torques Γ_x and Γ_y versus the azimuth angle for the case of $\theta_0 = 30°$. (**b**) The torques Γ_x and Γ_y versus the polar angle for the case of $\phi_0 = 30°$.

Figure 7a,b show the distributions of the optical torques in the x–y and y–z planes at the focus with $\theta_0 = \varphi_0 = 30°$, respectively. It can be seen that the total optical torque in the x–y plane is related to both Γ_x and Γ_y, while that in the y–z plane is only affected by Γ_y. The optical torque Γ_z disappears when the Rayleigh spheroidal particles are stably trapped, which means that the optical torque vector exists in the x–y plane. Figure 7c presents both the optical torque vector and the rotation trend of the Rayleigh spheroidal particle induced by the optical torque in the Cartesian coordinate system. The arrows "Γ", "ζ", and "κ" represent the directions of the optical torque, the major axis, and the rotation trend of the Rayleigh spheroidal particle, respectively; the dashed line in the x–y plane is the projection of the axis ζ. It can be seen that the optical torque is perpendicular to the plane composed of axes ζ and z, and this optical torque can make the major axis of the Rayleigh spheroidal particle rotate to the projection of axis ζ in the x–y plane. The stable trapping of Rayleigh spheroidal particles induced by the linear or radial polarized beams necessitates that the major axis of the particle coincides with the polarization direction of the linearly polarized beams or the optical axis of the radially polarized beam, respectively. In contrast, the stable trapping of Rayleigh spheroidal particles by HOVVBs can be achieved when the major axis of the Rayleigh spheroidal particle is parallel to the transverse plane. This means that HOVVBs can stably trap spheroidal Rayleigh particles in two-dimensional space instead of along a certain direction, and this discovery is useful for extending the degrees of freedom of control in optical micro-manipulation.
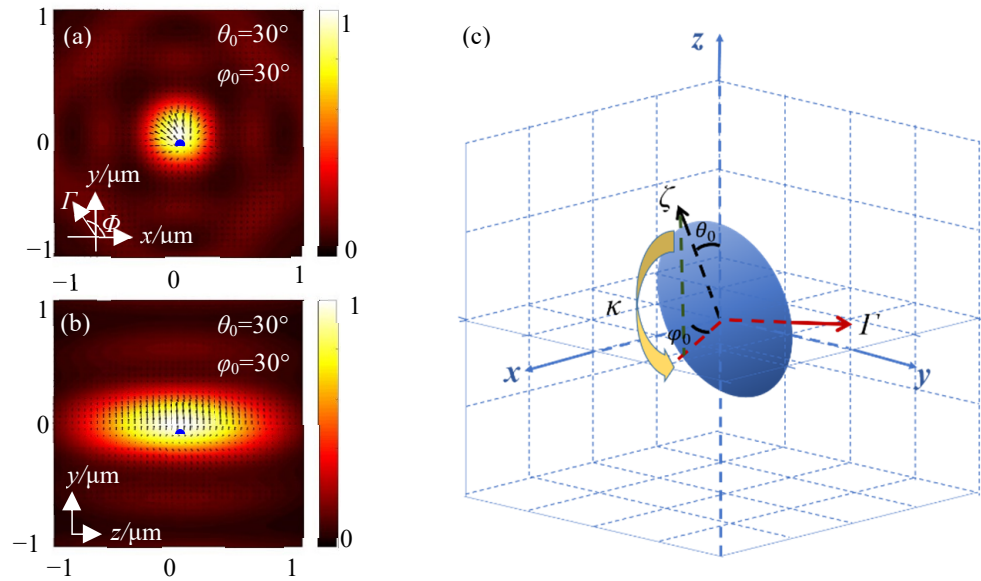
Figure 7. Optical torques in (**a**) the *x*–*y* plane and (**b**) the *y*–*z* plane at the focus. The blue point represents the position of the Rayleigh spheroidal particle. (**c**) Total optical torque and the corresponding rotation trend of the Rayleigh spheroidal particle.

The influences of the structural parameters of the Rayleigh spheroidal particle on the optical torque was studied. Figure 8a shows the evolution of the optical torque on the Rayleigh spheroidal particle with respect to its refractive index. It can be seen that the optical torque on the Rayleigh spheroidal particle increased with an increase in its refractive index, and the growth rate of the optical torque also gradually increased. This is because the polarizability of Rayleigh spheroidal particles increases with its refractive index; hence, the optical torque also increases. Figure 8b shows the evolution of the optical torque on the Rayleigh spheroidal particle with respect to its major semi-axis length when $n = 1.6$ and $b = 25$ nm. The optical torque was found to linearly increase with an increase in the major semi-axis length. Figure 8c presents the evolution of the optical torque on a Rayleigh spheroidal particle with respect to its minor semi-axis length when $n = 1.6$ and $a = 50$ nm. Similarly, the optical torque increases with the increase in the minor semi-axis length, and the growth rate of the optical torque also gradually increases. This is because the enlarging of the major and minor semi-axes of the Rayleigh spheroidal particle can enhance the beam scattering, resulting in an increase in the optical torque. Consequently, a large optical torque can be obtained for a large refractive index or longer major or minor semi-axes of Rayleigh spheroidal particles; this is useful for trapping and separating particles within a certain scope using tightly focused HOVVBs.
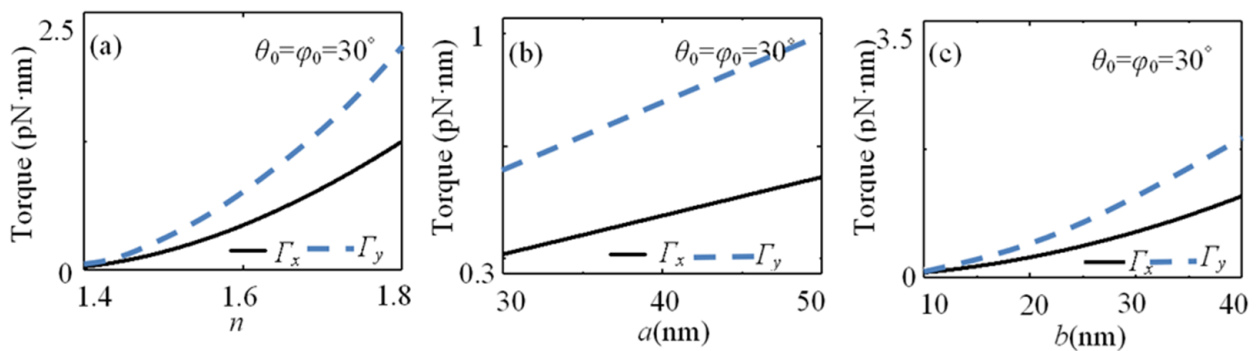
Figure 8. Variation in the optical torque with respect to the (**a**) refractive index, (**b**) major semi-axes length, and (**c**) minor semi-axes length of the Rayleigh spheroidal particle.

4. Conclusions

In summary, we utilized the advantages of HOVVBs, such as diverse intensity distributions at the focus and an adjustable longitudinal component, to achieve stable optical trapping of Rayleigh spheroidal particles. The optical forces and torques on Rayleigh spheroidal particles induced by the tightly focused HOVVBs with the polarization and phase topological charges of $|n| = |m|$ were analyzed based on the Rayleigh scattering model and dipole approximation. It was found that the HOVVBs could stably trap the Rayleigh spheroidal particle in the entire two-dimensional plane, which is unlike the linearly polarized and radial vector beams that can only trap in a certain direction. Furthermore, the optical torque Γ_x can achieve a maximum of 0.869 pN·nm at $\varphi_0 = 90°$ and $270°$, while Γ_y can achieve a maximum of 0.869 pN·nm at $\varphi_0 = 0°$ and $180°$ for the case $\theta_0 = 30°$. Both Γ_x and Γ_y can achieve the maxima at $\theta_0 = 45°$ and $135°$ (the maxima of Γ_x and Γ_y are 0.502 pN·nm and 0.869 pN·nm) for the case of $\varphi_0 = 30°$, and the evolution of Γ_x and Γ_y are dependent on $-\sin(2\theta_0)$ and $\sin(2\theta_0)$, respectively. To the best of our knowledge, this is the first report on the stable trapping of Rayleigh spheroidal particles in three dimensions simultaneously by using tightly focused HOVVBs. It is known that the particle's major axis must be in a specific direction when using regular beams to achieve optical trapping. In contrast, the proposed stable trapping of the Rayleigh spheroidal particle by using HOVVBs can be achieved when the major axis of the Rayleigh spheroidal particle is parallel to the transverse plane. HOVVBs are conducive for the large-scale stable trapping of Rayleigh spheroidal particles in the two-dimensional plane. We envision that our results could be utilized to extend the degrees of freedom of control of HOVVBs, which is beneficial for applications in the field of optical micro-manipulations.

Institutional Review Board Statement: Not applicable.

Informed Consent Statement: Not applicable.

Data Availability Statement: Not applicable.

Conflicts of Interest: The authors declare no conflict of interest.

References

1. Otte, E.; Denz, C. Optical trapping gets structure: Structured light for advanced optical manipulation. *Appl. Phys. Rev.* **2020**, *7*, 041308. [CrossRef]
2. Chuang, C.-H.; Ho, C.-Y.; Hsiao, Y.-C.; Chiu, C.-P.; Wei, M.-D. Selection rule for cavity configurations to generate cylindrical vector beams with low beam quality factor. *Opt. Express* **2021**, *29*, 5043–5054. [CrossRef] [PubMed]
3. Hu, H.; Luo, D.; Pan, C.; Qin, Y.; Zhang, Y.; Wei, D.; Chen, H.; Gao, H.; Li, F. Collapse of hybrid vector beam in Rb atomic vapor. *Opt. Lett.* **2021**, *46*, 2614–2617. [CrossRef]
4. Naidoo, D.; Fromager, M.; Ait-Ameur, K.; Forbes, A. Radially polarized cylindrical vector beams from a monolithic microchip laser. *Opt. Eng.* **2015**, *54*, 111304. [CrossRef]
5. Wang, B.; Che, Y.; Zhong, X.; Yan, W.; Zhang, T.; Chen, K.; Li, X. Cylindrical vector beam revealing multipolar nonlinear scattering for superlocalization of silicon nanostructures. *Photonics Res.* **2021**, *9*, 950–957. [CrossRef]
6. Niv, A.; Biener, G.; Kleiner, V.; Hasman, E. Manipulation of the Pancharatnam phase in vectorial vortices. *Opt. Express* **2006**, *14*, 4208–4220. [CrossRef] [PubMed]
7. Kang, M.; Chen, J.; Wang, X.-L.; Wang, H.-T. Twisted vector field from an inhomogeneous and anisotropic metamaterial. *J. Opt. Soc. Am. B* **2012**, *29*, 572–576. [CrossRef]

8. Mathieu, L.J.; Maurizio, R.; Romain, Q. Plasmon nano-optical tweezers. *Nat. Photonics* **2011**, *5*, 349–356.
9. Wu, M. Optoelectronic tweezers. *Nat. Photonics* **2011**, *5*, 322–324. [CrossRef]
10. Li, J.; Zheng, Y. Optothermally Assembled Nanostructures. *Acc. Mater. Res.* **2021**, *2*, 352–363. [CrossRef] [PubMed]
11. Li, J.; Chen, Z.; Liu, Y.; Kollipara, P.S.; Feng, Y.; Zhang, Z.; Zheng, Y. Opto-refrigerative tweezers. *Sci. Adv.* **2021**, *7*, eabh1101. [CrossRef] [PubMed]
12. Ashkin, A.; Dziedzic, J.M.; Bjorkholm, J.E.; Chu, S. Observation of a single-beam gradient force optical trap for dielectric particles. *Opt. Lett.* **1986**, *11*, 288–290. [CrossRef] [PubMed]
13. Zhan, Q. Trapping metallic Rayleigh particles with radial polarization. *Opt. Express* **2004**, *12*, 3377–3382. [CrossRef]
14. Jiang, Y.; Huang, K.; Lu, X. Radiation force of highly focused Lorentz-Gauss beams on a Rayleigh particle. *Opt. Express* **2011**, *19*, 9708–9713. [CrossRef] [PubMed]
15. Bi, L.; Yang, P.; Kattawar, G.W.; Kahn, R. Single-scattering properties of triaxial ellipsoidal particles for a size parameter range from the Rayleigh to geometric-optics regimes. *Appl. Opt.* **2008**, *48*, 114–126. [CrossRef]
16. Bekshaev, A.; Bliokh, K.; Soskin, M. Internal flows and energy circulation in light beams. *J. Opt.* **2011**, *13*, 053001. [CrossRef]
17. Wu, J.; Li, Y.; Lu, D.; Liu, Z.; Cheng, Z.; He, L. Measurement of the membrane elasticity of red blood cell with osmotic pressure by optical tweezers. *Cryo Lett.* **2009**, *30*, 89–95.
18. Bayoudh, S.; Nieminen, T.A.; Heckenberg, N.R.; Rubinsztein-Dunlop, H. Orientation of biological cells using plane-polarized Gaussian beam optical tweezers. *J. Mod. Opt.* **2003**, *50*, 1581–1590. [CrossRef]
19. Cherney, D.P.; Bridges, T.E.; Harris, J.M. Optical Trapping of Unilamellar Phospholipid Vesicles: Investigation of the Effect of Optical Forces on the Lipid Membrane Shape by Confocal-Raman Microscopy. *Anal. Chem.* **2004**, *76*, 4920–4928. [CrossRef]
20. Hinojosa-Alvarado, A.; Gutiérrez-Vega, J. Geometrical optics calculation of forces and torques produced by a ringed beam on a prolate spheroid. *J. Opt. Soc. Am. B* **2010**, *27*, 1651–1658. [CrossRef]
21. Cao, Y.; Song, W.; Ding, W.; Sun, F.; Zhu, T.; Zhu, T. Equilibrium orientations of oblate spheroidal particles in single tightly focused Gaussian beams. *Opt. Express* **2014**, *22*, 18113–18118. [CrossRef] [PubMed]
22. Xu, F.; Ren, K.; Gouesbet, G.; Cai, X.; Gréhan, G. Theoretical prediction of radiation pressure force exerted on a spheroid by an arbitrarily shaped beam. *Phys. Rev. E* **2007**, *75*, 026613. [CrossRef] [PubMed]
23. Rui, G.; Li, Y.; Zhou, S.; Wang, Y.; Gu, B.; Cui, Y.; Zhan, Q. Optically induced rotation of Rayleigh particles by arbitrary photonic spin. *Photon. Res.* **2018**, *7*, 69–79. [CrossRef]
24. Xu, F.; Lock, J.A.; Gouesbet, G.; Tropea, C. Radiation torque exerted on a spheroid: Analytical solution. *Phys. Rev. A* **2008**, *78*, 013843. [CrossRef]
25. Huang, K.; Shi, P.; Cao, G.W.; Li, K.; Zhang, X.B.; Li, Y.P. Vector-vortex Bessel–Gauss beams and their tightly focusing properties. *Opt. Lett.* **2011**, *36*, 888–890. [CrossRef]
26. Cui, Z.; Sun, J.; Litchinitser, N.M.; Han, Y. Dynamical characteristics of tightly focused vortex beams with different states of polarization. *J. Opt.* **2018**, *21*, 015401. [CrossRef]
27. Otte, E.; Tekce, K.; Denz, C. Tailored intensity landscapes by tight focusing of singular vector beams. *Opt. Express* **2017**, *25*, 20194–20201. [CrossRef]
28. Zou, X.; Zheng, Q.; Wu, D.; Lei, H. Controllable cellular micromotors based on optical tweezers. *Adv. Funct. Mater.* **2020**, *30*, 2002081. [CrossRef]
29. Vasse, G.F.; Buzón, P.; Melgert, B.N.; Roos, W.H.; van Rijn, P. Single Cell Reactomics: Real-Time Single-Cell Activation Kinetics of Optically Trapped Macrophages. *Small Methods* **2021**, *5*, 2000849. [CrossRef]
30. Hu, S.; Ye, J.-Y.; Zhao, Y.; Zhu, C.-L. Advanced optical tweezers on cell manipulation and analysis. *Eur. Phys. J. Plus* **2022**, *137*, 1024. [CrossRef]
31. Shen, Y.; Weitz, D.A.; Forde, N.R.; Shayegan, M. Line optical tweezers as controllable micromachines: Techniques and emerging trends. *Soft Matter* **2022**, *18*, 5359. [CrossRef]
32. Chen, H.; Lin, H.; Jones, P.H.; Chen, Z.; Luo, S.; Pu, J. Influence of slow light effect on trapping force in optical tweezers. *Opt. Lett.* **2022**, *47*, 710–713. [CrossRef] [PubMed]
33. Shao, M.; Zhong, M.C.; Wang, Z.; Ke, Z.; Zhong, Z.; Zhou, J. Non-Invasive Dynamic Reperfusion of Microvessels In Vivo Controlled by Optical Tweezers. *Front. Bioeng. Biotechnol.* **2022**, *10*, 952537. [CrossRef] [PubMed]
34. Hwang, H.; Byun, A.; Park, J.; de Léséleuc, S.; Ahn, J. Optical tweezers throw and catch single atoms. *Optica* **2023**, *10*, 401–406. [CrossRef]
35. Quy, H.Q.; Tuan, D.Q.; Thanh, T.D.; Thang, N.M. Enhance of optical trapping efficiency by nonlinear optical tweezers. *Opt. Commun.* **2018**, *427*, 341–347. [CrossRef]
36. Wei, W.; Zhu, L.; Tai, Y.; Li, X. Cycloid-structured optical tweezers. *Opt. Lett.* **2023**, *48*, 972–975. [CrossRef]
37. Richards, B.; Wolf, E. Electromagnetic diffraction in optical systems, II. Structure of the image field in an aplanatic system. *Royal Society* **1959**, *253*, 358–379.
38. Youngworth, K.; Brown, T. Focusing of high numerical aperture cylindrical-vector beams. *Opt. Express* **2000**, *7*, 77–87. [CrossRef] [PubMed]
39. Zhan, Q. Cylindrical vector beams: From mathematical concepts to applications. *Adv. Opt. Photonics* **2009**, *1*, 1–57. [CrossRef]
40. Li, M.; Yan, S.; Liang, Y.; Zhang, P.; Yao, B. Transverse spinning of particles in highly focused vector vortex beams. *Phys. Rev. A* **2017**, *95*, 053802. [CrossRef]

41. Zhao, Y.; Edgar, J.S.; Jeffries, G.D.M.; McGloin, D.; Chiu, D.T. Spin-to-Orbital Angular Momentum Conversion in a Strongly Focused Optical Beam. *Phys. Rev. Lett.* **2007**, *99*, 073901. [CrossRef]

42. Kotlyar, V.; Stafeev, S.; Zaitsev, V.; Kozlova, E. Spin-Orbital Conversion with the Tight Focus of an Axial Superposition of a High-Order Cylindrical Vector Beam and a Beam with Linear Polarization. *Micromachines* **2022**, *13*, 1112. [CrossRef]

43. Landau, L.D.; Lifshitz, E.M.; Sykes, J.B.; Bell, J.S.; Dill, E.H. Electrodynamics of Continuous Media. *Phys. Today* **1961**, *14*, 48–50. [CrossRef]

44. Simonot, L.; Hébert, M.; Hersch, R.D.; Garay, H. Ray scattering model for spherical transparent particles. *JOSA A* **2008**, *25*, 1521–1534. [CrossRef]

45. Mishchenko, M.I.; Yurkin, M.A. On the concept of random orientation in far-field electromagnetic scattering by nonspherical particles. *Opt. Lett.* **2017**, *42*, 494–497. [CrossRef] [PubMed]

46. Draine, B.T. The discrete-dipole approximation and its application to interstellar graphite grains. *Astrophys. J.* **1988**, *333*, 848–872. [CrossRef]

47. Li, M.; Yan, S.; Yao, B.; Lei, M.; Yang, Y.; Min, J.; Dan, D. Trapping of Rayleigh spheroidal particles by highly focused radially polarized beams. *J. Opt. Soc. Am. B* **2015**, *32*, 468–472. [CrossRef]

48. Li, M.; Yan, S.; Yao, B.; Liang, Y.; Han, G.; Zhang, P. Optical trapping force and torque on spheroidal Rayleigh particles with arbitrary spatial orientations. *JOSA A* **2016**, *33*, 1341–1347. [CrossRef]

49. Mitri, F.G. Optical Bessel beam illumination of a subwavelength prolate gold (Au) spheroid coated by a layer of plasmonic material: Radiation force, spin and orbital torques. *J. Phys. Commun.* **2017**, *1*, 015001. [CrossRef]

50. Chaumet, P.; Nieto-Vesperinas, M. Time-averaged total force on a dipolar sphere in an electromagnetic field. *Opt. Lett.* **2000**, *25*, 1065–1067. [CrossRef]